Organic-inorganic Hybrid Polyoxotungstates as Configurable Charge Carriers for High Energy Redox Flow Batteries

Catherine L. Peake, Alexander J. Kibler, Graham N. Newton* and Darren A. Walsh*

Nottingham Applied Materials and Interfaces (NAMI) Group, GSK Carbon Neutral Laboratories for Sustainable Chemistry, University of Nottingham, Jubilee Campus, Nottingham, NG7 2TU. graham.newton@nottingham.ac.uk darren.walsh@nottingham.ac.uk

ABSTRACT *We describe the synthesis and electrochemical analysis of the phenyl siloxane-hybridized phosphotungstate Keggin-type polyoxometalate (POM) $TBA_3[PW_{11}O_{39}(SiC_6H_5)_2O]$ (**$TBA_3W_{11}SiPh$**) and its performance as the charge carrier in non-aqueous redox flow batteries (RFBs). The hybridized POM is synthesized by modification of the parent POM $[PW_{12}O_{40}]^{3-}$, increasing its saturation concentration in acetonitrile by two orders of magnitude over that of parent compound (600 mmol dm^{-3} for **$TBA_3W_{11}SiPh$** vs. <1 mmol dm^{-3} for $TBA_3[PW_{12}O_{40}]$). Electrochemical analysis of **$TBA_3W_{11}SiPh$** reveals four one-electron, quasi-reversible, redox couples between –0.60 and –2.50 V vs. $Ag^+|Ag$, prompting us to explore its application as a dual-function charge carrier in symmetric RFBs. The stability of **$TBA_3W_{11}SiPh$** is investigated in several symmetric RFBs and the system demonstrates high coulombic efficiency (98%), voltage efficiency (89%) and energy efficiency (87%) during redox cycling. We show that capacity fade due to oxidation-state imbalance can be counteracted by re-reduction of electrolytes. These results demonstrate that organic-inorganic hybridisation of POMs offer opportunities for the development of highly soluble multi-electron redox electrolytes that operate across a wide range of potentials, expanding the available range of charge carriers for high-energy RFBs.*

KEYWORDS polyoxometalates; voltammetry; flow battery; electrolytes; galvanostatic analysis

Introduction

The integration of intermittent renewable energy sources into electrical-grid systems requires the development of high capacity, long-lived energy storage devices to minimize disruption to the grid supply.[1] In this respect, redox flow batteries (RFBs) are attracting a lot of attention for grid-scale applications. Energy is stored in charge carrier-containing electrolyte solutions that are pumped through electrodes to charge and discharge the cell. The electrolytes are separated in the electrochemical cell by a membrane or separator, which allows transfer of charge-balancing counter-ions across the cell but prevents cross-over of charge carriers. Their design favours long operational lifetimes and allows complete decoupling of capacity and power, enabling cost-effective scale-up.[2]

Despite their advantages, widespread uptake of RFBs is limited due to their cost and low energy density.[2,3] The most commercially advanced RFB system is the symmetric, all-vanadium RFB developed by Skyllas–Kazacos and co-workers in the late 1980s.[4] The charge carriers in the system are VO_2^+/VO^{2+} (V^{5+}/V^{4+}) in the positive electrolyte and V^{2+}/V^{3+} in the negative electrolyte. Despite rigorous efforts to improve performance, the all-vanadium RFB has several drawbacks. Firstly, its cost (*ca.* \$500/kWh in 2014)[5] is far higher than the US Department of Energy target of \$100/kWh[6] and is increasingly uncompetitive with lithium ion batteries (ca. \$156/kWh in 2020[2]). Secondly, the cell voltage of 1.3 V and limited solubility of vanadium sulfate in the aqueous acidic electrolyte limits the volumetric energy density of the system, E_V, to 20-35 Wh dm^{-3}.[7] E_V is defined in Equation 1:

$$E_V = \frac{nV_{cell}C_{active}F}{2} \quad (1)$$

where F is the Faraday constant, V_{cell} is the cell voltage, C_{active} is the concentration of charge carrier in the electrolyte, and n is the number of electrons transferred per molecule in the charge/discharge redox reaction.

These challenges have fuelled renewed interest in the development of new RFB chemistries. A diverse range of charge carriers, including metallocenes,[8] metal coordination complexes,[9] numerous organic molecules[10], and polyoxometalates (POMs), have been investigated.[11–14] POMs,

in particular, exhibit reversible multi-electron redox properties, making them especially promising charge carriers for high energy density RFBs.

The earliest work on POM RFBs was conducted by Anderson and co-workers, who used the tri-vanadium-substituted silicotungstate Keggin $[SiV_3W_9O_{40}]^{7-}$ as the positive and negative electrolytes in a symmetric aqueous system.[11] Subsequently, Stimming and colleagues used $[PV_{14}O_{42}]^{9-}$ and $[SiW_{12}O_{40}]^{4-}$ as the positive and negative electrolyte, respectively, in a aqueous asymmetric RFB.[12] Cycling in an upscaled cell (1400 cm^2 membrane surface area) over the course of almost 3 months showed good stability of this system.[15] In 2018, Cronin and colleagues reported a 225 Wh dm^{-3} aqueous asymmetric RFB containing $Li_6[P_2W_{18}O_{62}]$ as the negative electrolyte and HBr/Br_2 as the positive electrolyte.[13] In this case, the reversible reduction of $Li_6[P_2W_{18}O_{62}]$ by 18 electrons in aqueous acidic conditions demonstrated the opportunities offered by POMs for the development of high-E_V RFBs.

RFBs based on aqueous electrolyte, such as those highlighted above, are limited to a maximum V_{cell} of *ca.* 1.5 V, beyond which, electrolysis of water occurs. Non-aqueous electrolytes based on organic solvents and ionic liquids have been explored due to their higher electrochemical stability. Non-aqueous electrolytes also widen the scope of available charge carriers and open the opportunity to develop high-V_{cell} batteries.[16,17] However, without targeted modification, the solubility of POMs in non-aqueous solvent is limited. The first investigation of POMs in non-aqueous RFBs was conducted in 2013 by Anderson and colleagues. In an effort to enhance solubility, they conducted ion exchange of $K_6H[SiV_3W_9O_{40}]^{7-}$ to the corresponding tetrabutylammonium (TBA) salt, but found that the redox chemistry was electrochemically irreversible in propylene carbonate.[11] Barteau and co-workers demonstrated the first non-aqueous POM RFB with $Li_3[PMo_{12}O_{40}]$ in acetonitrile.[18] They later expanded the investigation to include an asymmetric POM/POM RFB based on $Li_3PMo_{12}O_{40}$ and $Li_6P_2W_{18}O_{62}$ in N,N-dimethylformamide as the positive and negative electrolytes, respectively.[19] The solubility of $Li_3[PMo_{12}O_{40}]$ was remarkably high at 1-1.2 mol dm^{-3}, but was compromised upon addition of supporting electrolyte.

Matson and co-workers demonstrated the use of vanadium oxide/alkoxide nanoclusters of the general formula $[V_6O_7(OR)_{12}]$ as the charge carriers in symmetric non-aqueous flow batteries.[20] The systems exhibit four 1-electron redox processes spanning *ca.* 2 V. In an effort to enhance solubility and cycling stability, several variations of ligand were explored to include alkoxides,[20] ethers,[21] tris-alkoxy (triol) derivatives[22] and mixed systems.[21] An impressive saturation concentration of 1.2 mol dm^{-3} in acetonitrile was reported for a mixed alkoxide/ether-functionalized polyoxovanadate.[23]

We seek to expand the concept of organofunctionalization of inorganic clusters to hybrid polyoxotungstates, to develop a new class of charge carriers for non-aqueous RFBs. This strategy offers enormous scope in selection of organic moity, covalent linker (phosphorus, silicon, germanium, or tin-based to name a few) and POM core (addenda metal, heteroatom, geometry) which presents a simple, modular approach to tune solubility, redox potential and electrochemical stability. The covalent linker plays an important role in governing the electronic properties of hybrid POMs[24], and allows for tunning of the charge carrier redox potentials. Organic-inorganic hybrid POMs have already been used in catalysis, energy materials and life sciences,[25] and can be further functionalized to yield novel soft redox materials.[26–31] Hybridisation can be applied to a broad range of POMs, which presents the opportunity to develop multi-electron charge carriers across a wide potential range. Successful implementation of this technique could enable high energy density asymmetric POM/POM non-aqueous RFBs.

We describe here the synthesis and characterization of the phosphotungstate Keggin siloxane hybrid POM $TBA_3[PW_{11}O_{39}(SiC_6H_5)_2O]$ (**$TBA_3W_{11}SiPh$**). This hybrid takes advantage of the multi-electron redox chemistry of the inorganic POM core and the solubility-enhancing properties of the organic moiety. The saturation concentration of **$TBA_3W_{11}SiPh$** in acetonitrile is two orders of magnitude higher than that of the parent molecule, $TBA_3[PW_{12}O_{40}]$ (**TBA_3W_{12}**). The electron donating nature of the siloxane linker slightly shifts the redox potential of the POM negatively.[32] The accessible oxidation states of **$TBA_3W_{11}SiPh$** span a ~2.0 V range, making them useful for symmetric RFBs. We show that a symmetric RFB containing **$TBA_3W_{11}SiPh$** has an average coulombic efficiency of 98%, voltage efficiency of 89%, and energy efficiency of 87% when cycled 75 times between 0.0 and 1.2 V. We also show that high-voltage symmetric RFBs that exploits the five accessible redox states of **$TBA_3W_{11}SiPh$** can be assembled by extending the voltage window to 2.0 V, but that the system deteriorates more rapidly than the lower-voltage system. We subsequently discuss the challenges involved in developing RFBs based on systems such as these, including the sensitivity of reduced **$TBA_3W_{11}SiPh$** to trace O_2, leading to electrolyte imbalance and capacity fade. We believe that these results enhance our understanding of the structure-property relationship of hybrid POMs and will guide synthetic approaches to design high performance RFBs containing non-aqueous electrolytes.

Experimental Section

Reagents and Apparatus. Electrochemical investigations were carried out in a N_2-filled glove box (MBraun, Garching, Germany; <0.1 ppm H_2O; <0.1 ppm O_2) at room temperature, using a Bio-Logic SP-300 potentiostat/galvanostat (Seyssinet-Parizet, France) run using EC-Lab software. Glassware and equipment were dried in a vacuum oven at 60 °C for 16 hours prior to use. Tetrabutylammonium hexafluorophosphate [TBA][PF_6] (≥ 99.0%, Sigma Aldrich) was used as received. Acetonitrile was degassed by several cycles of freezing under Ar, evacuation and thawing, before being dried over 4 Å molecular sieves (Sigma-Aldrich). ^1H NMR spectra were recorded using a Bruker BioSpin GmbH 400 MHz nuclear magnetic resonance spectrometer and referenced to the residual ^1H solvent signals. UV-visible spectroscopy of electrolytes was performed using an Agilent Cary UV-visible NIR spectrometer (Santa Clara, USA).

Synthesis of $TBA_3W_{11}SiPh$. The synthesis of **$TBA_3W_{11}SiPh$** was carried out using literature precedent.[30] Trichlorophenylsilane (0.44 cm^3, 2.7 mmol) was added to a solution of $(TBA)_4H_3[PW_{11}O_{39}]$ (5.0 g, 1.4 mmol) in acetonitrile (60 cm^3), stirred at room temperature for 15 hours, and then evaporated to dryness. The crude product was dissolved in the minimum possible volume of acetonitrile and precipitated by the addition of water. The product was isolated by centrifugation and washed with 1:1 volume ratio of diethyl ether : ethanol, to yield a pale-yellow powder (2.9 g, 57%). ^{1}H NMR (DMSO-d_6, 400 MHz): δ = 7.77 (m, 4.1H, CHAr), 7.51 (m, 6H, CHAr), 3.17 (m, 27.6H, NCH_2), 1.58 (m, 28.6H, CH_2), 1.32 (m, 29.3H, CH_2), 0.95 (t, J=7.3Hz, 43H, CH_2CH_3). ^{31}P{H} NMR (DMSO-d_6, 162 MHz): δ = −13.58. See Figures S1 and S2 for NMR spectra. Integration of peaks in the ^{1}H NMR indicated a slight excess of TBA cations (~0.5 equivalents). The discrepancy in TBA equivalents is due to a minor **TBA_3W_{12}** impurity as indicated by the peak at −15.60 ppm in the ^{31}P NMR. The impurity did not affect the electrochemical analysis substantially.

Cyclic Voltammetry. Cyclic voltammetry (CV) was carried out using a three-electrode cell, containing a 3 mm diameter glassy carbon (GC) working electrode (0.071 cm^2 surface area) and Pt wire auxiliary electrode (>0.16 cm^3 surface area). The reference electrode was a silver wire or $Ag^+|Ag$ non-aqueous reference electrode containing 10 mmol dm^{-3} $AgNO_3$ in 0.1 mol dm^{-3} [TBA][PF_6] in acetonitrile. The potential of the ferrocenium/ferrocene ($Fc^+|Fc$) redox couple was used as internal standard. The GC working electrode was polished using aqueous alumina slurries of decreasing particle size (1 μm, 0.3 μm and 0.05 μm), and rinsed thoroughly with water. The Pt wire auxiliary electrode was cleaned in a butane flame prior to use.

Bulk Electrolysis. Bulk electrolysis of electrolyte solutions was carried out in a purpose-built bulk electrolysis cell (BASi, Lafayette, USA) in a N_2-filled glove box. The cell contained a high surface area reticulated vitreous carbon working electrode, $Ag^+|Ag$ non-aqueous reference electrode, and Pt gauze counter electrode positioned behind a glass frit in 0.1 mol dm^{-3} [TBA][PF_6] in acetonitrile. The solution was stirred using a Teflon-coated stirrer bar. Constant-potential chronocoulometry was used to electrolyze the solution and UV-visible spectroscopy was used to follow oxidation of the electrolyte.

RFB Assembly. Flowing charge-discharge experiments were carried out in a N_2-filled glove box with 5 cm^2 membrane surface area RFB assembly (Scribner, Southern Pines, USA). Graphite felt electrodes (0.6 cm thickness, SGL carbon, Wiesbaden, Germany) were sandwiched between interdigitated graphite flow fields with PTFE flow frames and gaskets. A cation-exchange membrane (Fumasep F-930-RFD, Fumatech, Bietigheim-Bissingen, Germany) was used to separate the two half cells. Electrolytes comprised 10 mmol dm^{-3} **$TBA_3W_{11}SiPh$** in 0.5 mol dm^{-3} [TBA][PF_6] in acetonitrile were reduced to the desired oxidation state by bulk electrolysis. 15 cm^3 of electrolyte was placed in each reservoir. A dual-channel peristaltic pump (Masterflex L/S, Vernon Hills, USA) was used to pump electrolytes through the cell at a flow rate of 5 cm^3 min^{-1} using C-flex ULTRA tubing (Masterflex, Vernon Hills, USA). ±1 mA charge/discharge currents were used to test the cell performance.

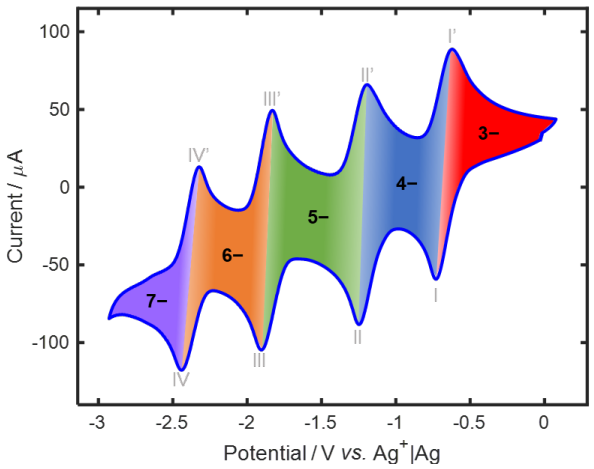

Figure 1. CV of 5 mmol dm^{-3} **$TBA_3W_{11}SiPh$** in 0.1 mol dm^{-3} [TBA][PF_6] in acetonitrile recorded using a GC working electrode (0.071 cm^2), Pt wire auxiliary electrode, and $Ag^+|Ag$ reference electrode. The scan rate was 0.1 V s^{-1}. Roman numerals denote the redox processes defined in equations 2-5. Colored areas denote the approximate regions of potential stability of **$TBA_3W_{11}SiPh$** in various oxidation states ($W_{11}SiPh^{3-}$, $W_{11}SiPh^{4-}$, $W_{11}SiPh^{5-}$, $W_{11}SiPh^{6-}$, and $W_{11}SiPh^{7-}$).

Results and discussion

Physical and Electrochemical Properties of $TBA_3W_{11}SiPh$. Saturated solutions of **$TBA_3W_{11}SiPh$** and **TBA_3W_{12}** in anhydrous acetonitrile were first prepared and diluted to a concentration detectable by UV-visible absorption spectroscopy. Concentrations were determined using a pre-prepared calibration and back calculated to determine the saturation concentration of each POM (Figure S3). The saturation concentration of the hybrid **$TBA_3W_{11}SiPh$** in the organic solvent was 600 mmol dm^{-3}, compared to <1 mmol dm^{-3} for the parent **TBA_3W_{12}**.

While there are some examples of POM solubility >600 mmol dm^{-3} in non-aqueous solvents[19,23], organic-inorganic hybridisation is a solubility-enhancing technique that is applicable to a wide range of POM structures.[24] The flexibility in selection of POM metal-oxide core (elemental composition and size), covalent linker and organic moiety, provides a powerful technique for tailoring properties of multi-electron charge carriers for RFBs.

Figure 1 shows a cyclic voltammogram (CV) of **$TBA_3W_{11}SiPh$** dissolved in acetonitrile containing 0.1 mol dm^{-3} [TBA][PF_6] as electrolyte, recorded using a polished GC working electrode and a scan rate, v, of 0.1 V s^{-1}. Four reduction processes (labelled I – IV, from positive to negative potentials) are observed and correspond to four 1-electron processes (equations 2 – 5). The corresponding oxidation process are labelled I' – IV'. The redox couples accessed during the voltammetric experiment are as follows:

$$\text{I/I':} \quad W_{11}SiPh^{3-} + e^- \rightleftharpoons W_{11}SiPh^{4-} \qquad (2)$$

$$\text{II/II':} \quad W_{11}SiPh^{4-} + e^- \rightleftharpoons W_{11}SiPh^{5-} \qquad (3)$$

III/III': $W_{11}SiPh^{5-} + e^- \rightleftharpoons W_{11}SiPh^{6-}$ (4)

IV/IV': $W_{11}SiPh^{6-} + e^- \rightleftharpoons W_{11}SiPh^{7-}$ (5)

The mid-point potential, E_{mid}, peak-to-peak separation, ΔE_p, and ratio of anodic to cathodic peak currents, $i_{p,a}/i_{p,c}$, of each redox couple are provided in Table 1. These data are in good agreement with the values found in the literature.[30] $i_{p,a}/i_{p,c}$ is close to unity for each redox couple, as expected for an electrochemically-reversible redox couple. However, ΔE_p for processes I/I', III/III' and IV/IV' is greater than the value of 59 mV expected for the electrically-reversible transfer of a single electron. Moreover, ΔE_p increased as the voltammetric scan rate increased, indicating that each redox process was electrochemically quasi-reversible.

Table 1. E_{mid}, ΔE_p, and $i_{p,a}/i_{p,c}$ determined from cyclic voltammetry of **$TBA_3W_{11}SiPh$** recorded at 0.1 V s^{-1}.

Process	E_{mid} / V	ΔE_p / mV	$i_{p,a}/i_{p,c}$
I/I'	−0.66	106	0.96
II/II'	−1.18	58	1.12
III/III'	−1.81	70	0.97
IV/IV'	−2.31	122	1.00

All potentials are reported *vs.* that of an $Ag^+|Ag$ reference electrode. $E_{mid} = (E_c + E_a)/2$, where E_c = cathodic peak potential and E_a = anodic peak potential

Fast mass transport and electron transfer of charge carriers is key to enabling high power density RFBs. We determined the diffusion coefficient, D, and heterogeneous electron transfer rate constant, k^0, of **$TBA_3W_{11}SiPh$** by investigating the effect of v on the voltammetric response (Figures S4 - Figure S6). At v > 50 mV s^{-1}, the plot of $i_{p,c}$ *vs.* $v^{1/2}$ for process I deviated from linearity, so the gradient in the region 10 mV s^{-1} < v < 50 mV s^{-1} was used (Figure S5) in conjunction with Equation 6 to estimate D_0:[33]

$$i_p = 2.99\times10^5\, n^{3/2}\, \alpha^{1/2}\, D^{1/2}\, C\, A\, v^{1/2} \quad (6)$$

where α is the transfer coefficient and is assumed to be 0.5, A is surface area of the electrode (0.071 cm^2), C is the bulk concentration (5 mmol dm^{-3}), and n is the number of electrons transferred (1). Our analysis reveals that, despite its relatively large size, D of **$TBA_3W_{11}SiPh$** = 2.3 × 10^{-5} cm^2 s^{-1}. The organic functionality of **$TBA_3W_{11}SiPh$** allows for application of diffusion ordered NMR spectroscopy (DOSY NMR) to calculate D in acetonitrile. The aromatic signals decay similarly with a D of 1.2 × 10^{-5} cm^2 s^{-1}, which corresponds well with that determined electrochemically. The value of D calculated by DOSY NMR is an order of magnitude greater than functionalised polyoxovanadates investigated by Matson and colleagues (~1.5 × 10^{-6} cm^2 s^{-1})[14] and of vanadium sulphate in aqueous electrolyte[34] and vanadium acetylacetonate in acetonitrile.[35]

The Nicholson method was used to estimate k^0 for reduction/oxidation of **$TBA_3W_{11}SiPh$**.[36] The dimensionless parameter, Ψ, was obtained from the literature based on ΔE_p for process I/I' in Figure 1, and k^0 was extracted from the gradient of the plot of Ψ *vs.* $[\pi DnF/RT]^{-1/2}$, within the range 100 < v < 500 mV s^{-1} and in conjunction with Equation 7 (Figure S6):

$$\Psi = k^0 \left[\frac{\pi D F}{RT}\right]^{-1/2} v^{-1/2} \quad (7)$$

where R is the ideal gas constant and T is the absolute temperature. Using this analysis and the D value attained from DOSY NMR, k^0 was estimated at 2.5 × 10^{-2} cm s^{-1}, which is higher than that of the VO_2^+/VO^{2+} and V^{3+}/V^{2+} couples used in the all-vanadium RFB (~10^{-5} cm s^{-1}).[34] Extended potential cycling was used as an initial assessment of electrochemical stability. After 30s cycles in the potential range −3.0-0.0 V, the CV shape remained unchanged (Figure S7), demonstrating that **$TBA_3W_{11}SiPh$** was stable during repeated redox cycling.

Comparison of the CV of **$TBA_3W_{11}SiPh$** to that of the non-hybridized analogue **TBA_3W_{12}**, revealed an 80 mV

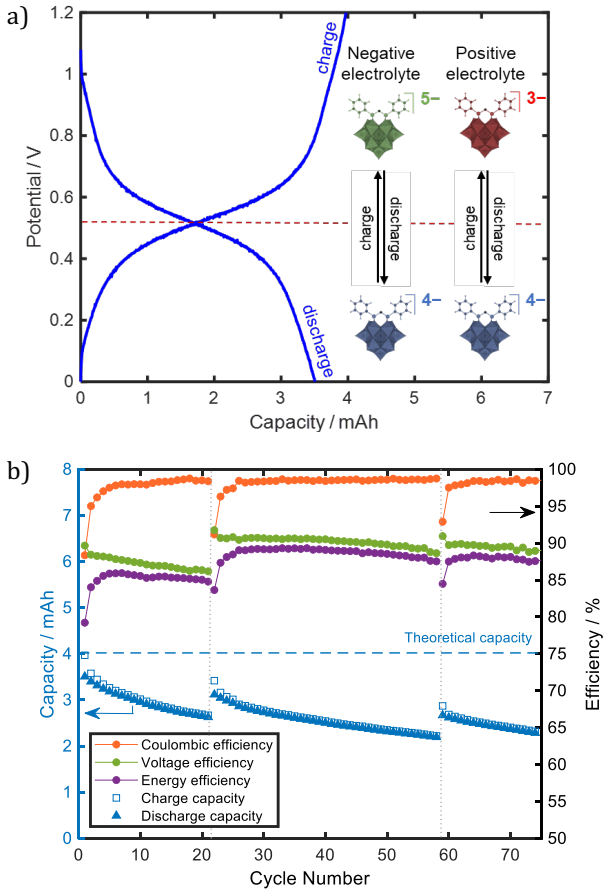

Figure 2. Galvanostatic charge-discharge analysis of a cell containing 10 mmol dm^{-3} $W_{11}SiPh^{4-}$ in 0.5 mol dm^{-3} [TBA][PF_6] in acetonitrile in the voltage range 0-1.2 V. Half cells were separated by a cation exchange membrane with charge/discharge current of ±1 mA (C-rate of 0.25) and flow rate of 5 cm^3 min^{-1}. a) Charge/discharge profile of cycle 1 b) capacity and efficiency values per cycle (electrolyte regeneration after cycle 21 and 58 is denoted by dotted grey lines).

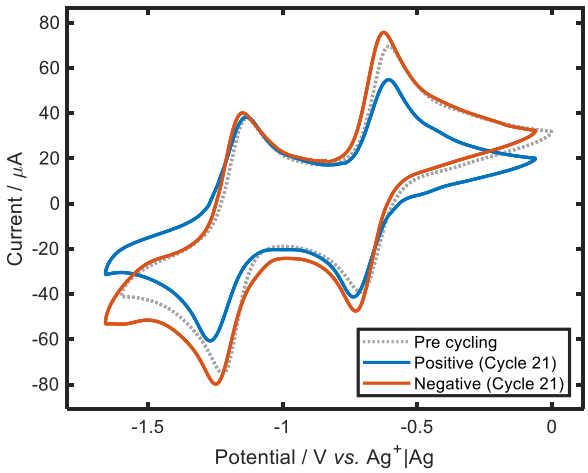

Figure 3. CV of positive and negative electrolyte after 21 charge/discharge cycles in the $W_{11}SiPh^{4-}$-based RFB (cycling data shown in Figure 2). The blue and red lines are the responses for the positive and negative electrolyte, respectively. The dotted line is the response obtained before charge/discharge analysis. CVs were recorded using a GC working electrode (0.071 cm^2), a Pt wire counter electrode, and $Ag^+|Ag$ reference electrode, at a scan rate of 50 mV s^{-1}.

negative shift in onset potential of process I after hybridisation (Figure S8). This is attributed to the electron-donating nature of the siloxane group and demonstrates the ability of hybridisation to influence the LUMO energy level of the redox centre, in addition to the POM solubility.[32]

RFB Performance. The use of the same charge carrier in each electrolyte of the RFB (that is, the use of symmetric cells) minimizes the complexity of the system. Moreover, while some membrane cross-over is inevitable with the imperfect separators available, symmetric systems have the advantage that charge carriers migrated to the opposite side can be recharged in the subsequent charge cycle, preventing permanent capacity loss. Here we present charge/discharge cycling results of several symmetric RFBs. The first RFB is termed Flow1 and exploits **$TBA_3W_{11}SiPh$** in its $W_{11}SiPh^{3-}$, $W_{11}SiPh^{4-}$, and $W_{11}SiPh^{5-}$ states. The second cell is termed Flow2 and exploits **$TBA_3W_{11}SiPh$** in its $W_{11}SiPh^{3-}$, $W_{11}SiPh^{4-}$, $W_{11}SiPh^{5-}$, $W_{11}SiPh^{6-}$, and $W_{11}SiPh^{7-}$ states (Equations 2-5).

RFB cycling of Flow1. An electrolyte consisting of 10 mmol dm^{-3} **$TBA_3W_{11}SiPh$** in 0.5 mol dm^{-3} [TBA][PF_6] in acetonitrile was electrochemically pre-reduced by one electron per POM, from an open circuit potential (OCP) of −0.05 to −0.95 V *vs.* $Ag^+|Ag$. 15 cm^3 of this $W_{11}SiPh^{4-}$ electrolyte was added to both reservoirs of the RFB. We conducted galvanostatic cycling within the potential window 0.0-1.2 V at a C-rate of 0.25 (±1 mA) based on the theoretical capacity of 4.02 mAh.

The charge/discharge reactions at the positive and negative electrolyte correspond to those in Equations 2 and 3 for processes I/I' and II/II', respectively. Single charge and discharge plateaus were observed for the initial cycle at ~0.55 V (Figure 2a), closely corresponding to the value expected from the difference in the E_{mid} of processes I/I' and II/II' (Table 1). The charge/discharge plateau at 0.55 V remained consistent over the course of 75 cycles and >440 hours. The initial charge cycle achieved an electrochemical yield (percentage of theoretical capacity achieved upon charge) of 99%. However, the electrochemical yield decreased by 22% over the course of the initial 10 cycles (Figure 2b blue open squares). The capacity fade was significant for the initial cycles and quickly stabilized to an average drop of 0.5% per cycle.

There are several physical and chemical factors that could contribute to the observed capacity loss, including degradation, precipitation or oxidation of **$TBA_3W_{11}SiPh$**, asymmetric membrane cross-over (preferential in one direction), electrolyte leakage, or unwanted side reactions. Several studies have offered experimental methodologies to determine the source of capacity fade in novel RFB systems.[37,38] No electrolyte leakage or charge carrier precipitation was observed during the cycling experiment. In order to investigate the cause of capacity fade, discharged electrolytes were removed from the cell after 21 cycles and were analysed using cyclic voltammetry. The shapes of the CVs of positive and negative electrolyte before and after cycling (Figure 3) were broadly similar, indicating that $W_{11}SiPh^{3-}$, $W_{11}SiPh^{4-}$, and $W_{11}SiPh^{5-}$ were stable during electrochemical cycling, but the background currents differed. While this obviously does not demonstrate that redox-inactive degradation products had formed, it does indicate that the redox chemistry of **$TBA_3W_{11}SiPh$** remains stable to cycling between the oxidised and two-electron reduced states.

To determine the cause of capacity fade upon cycling, the discharged positive and negative electrolytes (after 21 cycles and 140 hours of cycling) were further investigated in a three-electrode cell. We observed a positive shift in open-circuit potential (OCP) of discharged electrolytes post cycling. The OCP increased from −0.95 V (pre cycling) to −0.74 V and −0.80 V (post 21 cycles) for the positive and negative electrolyte, respectively, indicating that the electrolytes had undergone a net oxidation over the course of cycling. Despite being assembled in a N_2-filled glove box, we hypothesized that trace amounts of O_2 in the solvent and atmosphere are responsible for the oxidation of the POM (Figure S9). This net oxidation causes a reduction in the concentration of charge carrier in an oxidation state available to undergo charge. Stimming and co-workers observed a similar phenomenon in an aqueous POM-based RFBs, in which $[PV_{14}O_{42}]^{9-}$ in the positive electrolyte underwent a net oxidation by residual O_2 in the system.[39]

Stimming and colleagues were able to demonstrate regeneration of lost capacity through injection of the chemical reductant, hydrazine. In a similar vein, we were able to regain lost capacity through electrochemical re-reduction of electrolytes. Electrolytes were removed from the battery and re-reduced to the target potential of −0.95 V before being returned to their respective reservoirs without alteration to the membrane or electrodes. The RFB with regenerated electrolyte (Cycle 22 onwards, Figure 2b) regained its lost capacity, with the electrochemical yield returning to 86%. Due to the scale of these experiments, we believe that small volumes of liquid lost in the transfer of electrolyte between the RFB and bulk electrolysis assemblies, account for the incomplete capacity regain. These results indicate that the primary cause of capacity fade is

electrolyte imbalance and not structural degradation of the POM.

After 350 hours of cycling, we observed a discrepancy in electrolyte volume in the positive and negative electrolytes. Upon disassembly of the cell, we also observed a difference between positive and negative electrolyte in the mass of residual solids ([TBA][PF_6] and **$TBA_3W_{11}SiPh$**) after solvent removal. This was attributed to asymmetric membrane cross-over and is a secondary cause of capacity fade in this system. After 58 cycles, discharged positive and negative electrolytes were removed from the RFB and mixed together before being equally redistributed to the electrolyte reservoirs without altering the RFB assembly. The RFB with rebalanced electrolytes (Cycle 59, onwards, Figure 2b) again showed some regeneration of lost capacity. Barteau and colleagues reported good selectivity of an aramid nanofiber membrane in POM-based non-aqueous RFBs which separates electrolytes based on size-exclusion,[18] offering a possible route to solving this source of capacity fade in our system.

The challenges involving electrolyte imbalance notwithstanding, our RFB exhibited an average coulombic efficiency, CE (discharge capacity divided by charge capacity), of 98% over 75 cycles, demonstrating that electron transfer to and from the hybrid POM was reversible (Figure 2b). The RFB also displayed consistently high energy efficiency, EE (discharge energy divided by charge energy) and voltage efficiency, VE (EE divided by CE), averaging 87% and 89% respectively over the 75 cycles.

To assess the impact of asymmetric membrane cross-over more closely, a second Flow1 experiment was assembled under the same conditions, but the potential thresholds were alternated between 0.0 and 1.2 V and 0.0 and −1.2V for a given cycle. This has the effect of alternating which reservoir is the effective positive and negative electrolyte, thereby minimizing the concentration imbalanced caused by asymmetric membrane cross-over. Over the course of 17 cycles, the alternating cell showed a capacity fade of approximately 14%. In contrast, the standard cell exhibited a capacity loss of approximately 33%. The improved capacity retention demonstrated by the alternating cell suggests that crossover is a significant source of capacity loss under standard conditions. It is quite clear that changing the positive and negative electrolytes during cycling did not completely eliminate capacity fade from the cell and the residual can at least in part be attributed to oxidation of electrolytes by trace O_2 and even potentially H_2O in the cell.

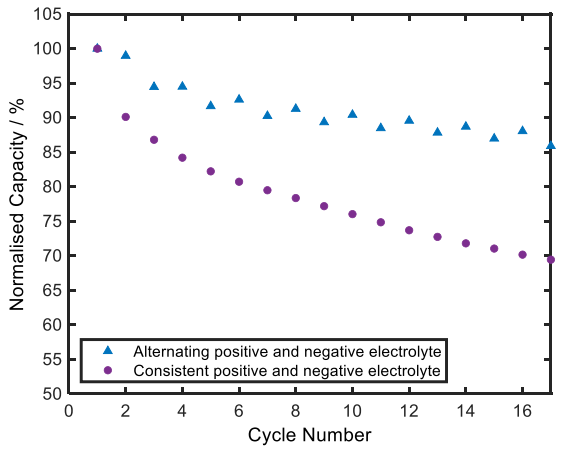

Figure 4. Comparison of Flow1 (purple circles) and Flow1 alternating (blue triangles). Capacity was normalised to cycle 1 charge capacity. All other conditions were kept consistent.

It is important to note that, while beyond the scope of this work, the ability of **$TBA_3W_{11}SiPh$** to reversibly exchange up to 4 electrons at highly negative potentials is potentially advantageous for use as negative electrolyte in asymmetric RFBs. Coupled with a high-potential positive electrolyte, **$TBA_3W_{11}SiPh$** could generate a high voltage and high energy density RFB. Moreover, such an approach could lessen the impact of O_2 ingress on capacity retention. The negative electrolyte in the symmetric systems investigated here is held in reduced states when charged and discharged, making it susceptible to capacity loss by oxidation at all times. As negative electrolyte in an asymmetric system **$TBA_3W_{11}SiPh$** could be reduced upon

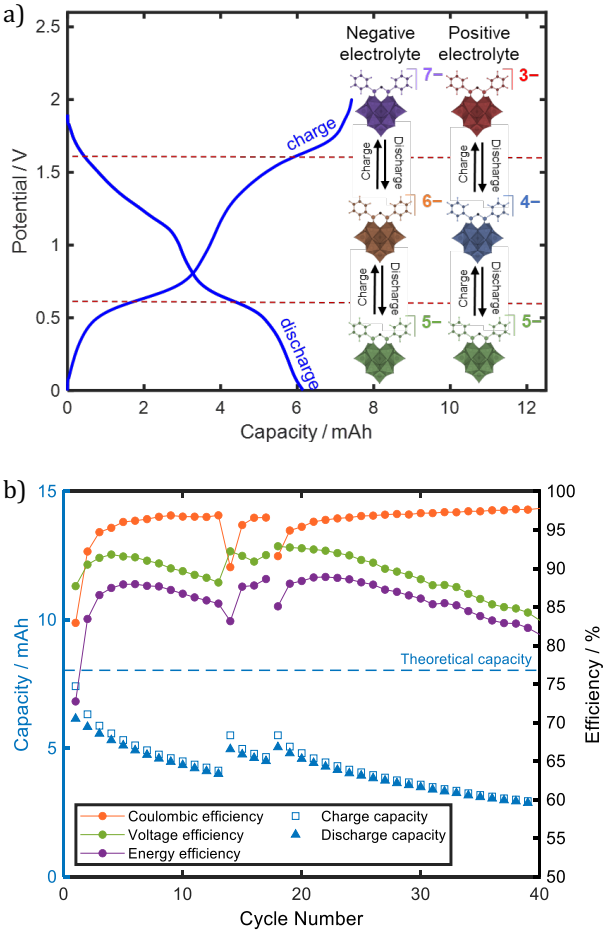

Figure 5. Symmetric RFB investigation (Flow2) of 10 mmol dm^{-3} $W_{11}SiPh^{5-}$ in 0.5 mol dm^{-3} [TBA][PF_6] in acetonitrile within the voltage threshold of 0 to 2.0 V. Half cells were separated by a cation exchange membrane with charge/discharge current of ±1 mA (C-rate of 0.125) and flow rate of 5 cm^3 min^{-1}. a) Charge/discharge profile of cycle 1 b) capacity and efficiency values per cycle (cycles 1-40 shown only).

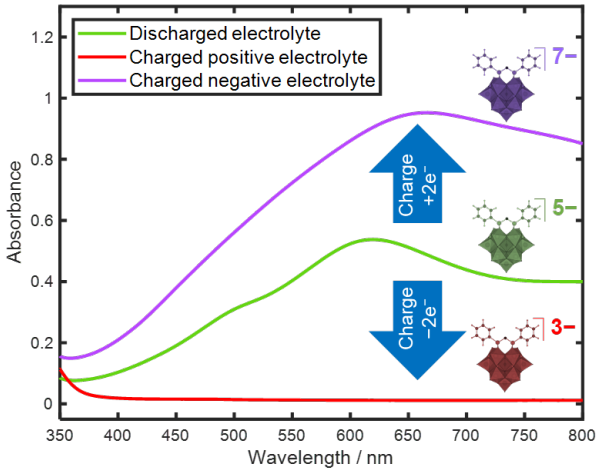

Figure 6. UV-visible absorption spectra of discharge electrolyte (green), charged positive electrolyte (red), and charged negative electrolyte (purple).

charge and reoxidized to the air-stable $W_{11}SiPh^{3-}$ state when fully discharged, potentially combating this source of capacity fade.

RFB cycling of Flow2. We designed a second RFB to investigate whether all five accessible states of **$TBA_3W_{11}SiPh$** (described by Equations 2-5) could be exploited, potentially increasing E_V. An electrolyte consisting of 10 mmol dm^{-3} **$TBA_3W_{11}SiPh$** in 0.5 mol dm^{-3} [TBA][PF_6] in acetonitrile was prepared and pre-reduced by two electrons per POM, from an OCP of −0.05 to −1.45 V *vs.* $Ag^+|Ag$. 15 cm^3 of $W_{11}SiPh^{5-}$ electrolyte was added to each reservoir of the RFB. We conducted galvanostatic cycling within the potential window 0.0-2.0 V at a C-rate of 0.125 (±1 mA) based on the theoretical capacity of 8.04 mAh. The proposed charge and discharge reactions in the negative and positive electrolytes of this cell are those given Equations 3 and 2 in the positive electrolyte and 4 and 5 in the negative electrolyte. Upon charging the cell, two charge plateaus were observed at potentials of ~0.6 V and ~1.6 V (Figure 5a). These values closely correspond to those expected from the difference in E_{mid} of the redox process in Table 1. Two plateaus are observed upon discharge. The first is a sloping plateau between 1.8 and 1.0 V and the second is more defined plateau at ~0.6 V.

The effects of charging and discharging the cell on the states of the charge carriers were examined using UV-visible absorption spectroscopy. Electrolyte was sampled from the reservoirs of the RFB when charged and discharged and diluted in acetonitrile by a factor of 100 for analysis. Figure 6 shows the overlayed spectra of discharged electrolyte (before cycling) and charged positive and negative electrolyte. The broad absorbance maxima at 620 nm and the shoulder peak at 500 nm observed for electrolyte in the discharged state (green) is characteristic of the $W^V \rightarrow W^{VI}$ intervalence charge transfer bands (ICVT) expected for a two-electron reduced phosphotungstate Keggin[40] and confirms that $W_{11}SiPh^{5-}$ is the dominant state. Spectroelectrochemical analysis of **$W_{11}SiPh$** (Figure S10) supports this observation. The charged positive electrolyte (red) is a colorless solution and shows negligible absorbance in the visible region. This confirms that the positive electrolyte was fully oxidized to $W_{11}SiPh^{3-}$ upon charging. A broad and intense peak with an absorbance maximum at 665 nm is observed in the spectrum of the charged negative electrolyte (purple). While spectroelectrochemical analysis was not extended to the four-electron reduced state, the increase in absorbance and shift in maxima beyond that of $W_{11}SiPh^{6-}$ (635 nm) is consistent with the presence of the $W_{11}SiPh^{7-}$ state in solution.

Figure 5b shows the charge and discharge capacities and efficiency of cycling for the initial 40 cycles of Flow2. The initial charge cycle achieved an electrochemical yield of 92%, which decreased by 36% over the course of the first 10 cycles (Figure 5b blue open squares). By cycle 10, the shape of charge/discharge profiles had changed significantly. While the plateaus at 0.6 V remained consistent, the plateaus at 1.6 V were no longer observed and were replaced by charge/discharge plateaus at ~1.2 V (Figure 7, orange lines). Given that UV-visible spectroscopy confirmed that the positive electrolyte was oxidized to $W_{11}SiPh^{3-}$ on charging, the drop in the charging potential appears to be associated with decay or loss of the highly-reduced states. Once stabilized, high CE was achieved averaging >97% over the course of 92 cycles. A general decrease in VE and EE was observed with cycling but remained relatively high, averaging 79% and 77 % respectively over the course of 92 cycles (Figure 5b).

After 17 cycles, electrolytes were removed from the RFB and analysed. The OCPs of discharged electrolytes were measured and again indicated that the positive and negative electrolyte had been oxidized; OCP increased to −1.07 V and −1.08 V, respectively. The higher rate of capacity fade observed for Flow2 compared to Flow1 can in part be explained by the increased driving force for oxidation of $W_{11}SiPh^{7-}$ compared to that of $W_{11}SiPh^{5-}$. Electrolytes were regenerated by bulk electrolysis in the same means as described above. While some capacity was regained (Cycle 18 onwards, Figure 5b), it is clear that

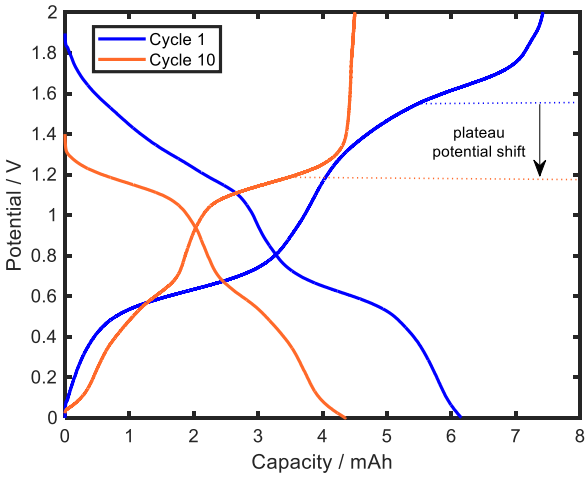

Figure 7. Symmetric RFB investigation (Flow2) of 10 mmol dm^{-3} **$W_{11}SiPh^{5-}$** in 0.5 mol dm^{-3} [TBA][PF_6] in acetonitrile within the voltage threshold of 0 to 2.0 V. Half cells were separated by a cation exchange membrane with charge/discharge current of ±1 mA (C-rate of 0.125) and flow rate of 5 cm^3 min^{-1}. a) Charge/discharge profile of cycle 1 and cycle 10.

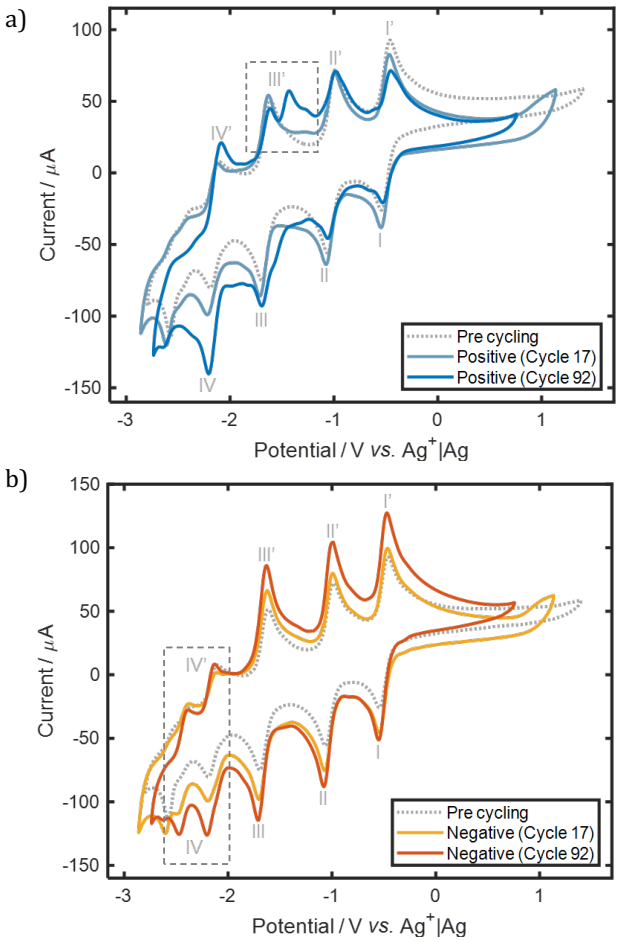

Figure 8. CV of a) positive and b) negative electrolyte after 17 cycles (185 h) and 92 cycles (610 h) in the $W_{11}SiPh^{5-}$-based RFB (cycling data shown in Figure 4). The dotted line is the response obtained before charge/discharge analysis. CV recorded at a GC working electrode (0.071 cm^2), with Pt wire counter electrode and $Ag^+|Ag$ reference electrode, at a scan rate of 50 mV s^{-1}.

imbalance of electrolytes was not the only cause for capacity fade in this RFB.

Cyclic voltammetry of the electrolytes before and after bulk electrolysis to the $W_{11}SiPh^{5-}$ state (Figure S11) and of the positive and negative electrolyte following 17 and 92 cycles in the RFB (Figure 8) was compared to explore degradation of the cell behaviour further. After bulk electrolysis to the $W_{11}SiPh^{5-}$ state, the peak for processes IV/IV' decreased in comparison to those of the other three redox processes and an irreversible reduction peak appeared at −2.57 V *vs.* Ag+|Ag (dotted lines in Figure 8). The CV of the negative electrolyte following RFB cycling (Figure 8b orange and yellow lines) also showed splitting of process IV/IV' into two distinct redox couples each with comparatively low peak currents. The CV of the positive electrolyte following RFB cycling (Figure 8a blue lines) shows that process III/III' had split into two peaks. Variation in current magnitude in the CVs of electrolytes sampled over the course of battery cycling can be expected due to an increase in electrolyte concentration over time as solvent evaporation occurs. It is important to note that the instability of processes III/III' and IV/IV' are not observed during repeated analytical voltammetry of the **$TBA_3W_{11}SiPh$** (Figure 1). The instability of process IV/IV', in particular, seems to be related to the formation of by-products during our preparative bulk electrolysis (Figure S11). In addition, NMR spectroscopy indicated that some speciation of **$TBA_3W_{11}SiPh$** had occurred upon bulk electrolysis to the two-electron reduced state, as indicated by several new peaks in the ^{31}P NMR spectrum (Figure S12). NMR spectroscopy of the positive and negative electrolytes following 92 potential cycles did not indicate any further degradation of **$TBA_3W_{11}SiPh$** upon cycling (Figure S13), so the changes in the POM were primarily associated with bulk electrolysis. In summary, while these data demonstrate the opportunities offered by the formation of the highly-reduced forms of **$TBA_3W_{11}SiPh$** for the development of high-capacity RFBs, future work should focus on the development of efficient methods for synthesizing the $W_{11}SiPh^{5-}$ form of the POM for the discharged cell.

CONCLUSIONS

In this work, we presented an approach to tuning the redox potential and solubility of polyoxometalates for use in high energy non-aqueous redox-flow batteries. The phosphotungstate Keggin siloxane hybrid POM **$TBA_3W_{11}SiPh$** investigated in this study is more soluble than its non-hybridized analogue by two orders of magnitude. We investigated the performance of **$TBA_3W_{11}SiPh$** as multi-electron charge carrier in two symmetric non-aqueous RFBs where **$TBA_3W_{11}SiPh$** in different oxidation states was used as both positive and negative electrolyte. Given the saturation concentration of 600 mmol dm^{-3}, average cell voltage of 1.1 V and two-electron redox reaction, the theoretical energy density of the symmetric **$TBA_3W_{11}SiPh$**-based RFB is 17.7 Wh dm^{-3}. Our RFBs were cycled for 75 cycles (>440 hours) with high coulombic efficiency, but capacity fade was observed upon cycling. The capacity fade was attributed to oxidation of the POMs by trace O_2 contamination in the system and migration of electrolyte through the membrane to the negative half-cell causing a concentration imbalance between electrolytes and reduced capacity. These causes of capacity fade could be reversed through bulk electrolysis or mixing of the electrolytes. A third cause of capacity fade was the instability of **$TBA_3W_{11}SiPh$** when reduced by five electrons per POM. Future work will focus on stabilizing such highly-reduced forms of the POM, especially considering the potential payoff in terms of the development of high-energy RFBs based on such systems. The advantage of using these hybrid materials as charge carriers in RFBs is their synthetic flexibility; the metal-oxide core, covalent linker, and organic groups of these systems can all be readily tuned offering numerous opportunities for optimisation of these novel charge carriers for RFBs.

AUTHOR INFORMATION

Corresponding Author

*Darren A. Walsh – Nottingham Applied Materials and Interfaces (NAMI) Group, GSK Carbon Neutral Laboratories for Sustainable Chemistry, University of Nottingham, Jubilee

Campus, Nottingham, NG7 2TU, United Kingdom; ORCID: 0000-0003-3691-6734; Email: darren.walsh@nottingham.ac.uk
*Graham N. Newton – Nottingham Applied Materials and Interfaces (NAMI) Group, GSK Carbon Neutral Laboratories for Sustainable Chemistry, University of Nottingham, Jubilee Campus, Nottingham, NG7 2TU, United Kingdom; ORCID: 0000-0003-2246-4466; Email: graham.newton@nottingham.ac.uk

Author Contributions

CLP performed the experimental work and wrote the manuscript. AJK helped in the charge carrier preparation and characterization. DAW and GNN conceived the project and co-wrote the manuscript. All authors have given approval to the final version of the manuscript.

Notes

The authors declare no conflict of interest.

ASSOCIATED CONTENT

Supporting Information

The supporting information is available free of charge via the Internet at http://pubs.acs.org. Nuclear magnetic resonance spectroscopic analysis, diffusion coefficient determination, electron transfer rate constant evaluation, and studies on the electrolytes.

ACKNOWLEDGMENTS

CLP thanks the Engineering and Physical Sciences Research Council (EPSRC) for funding through the Centre for Doctoral Training in Sustainable Chemistry (EP/L015633/1). DAW thanks the EPSRC for funding through project EP/P002382/1. GNN and DAW thank CAM-IES for support. All authors thank the EPSRC for funding through the INPOMS programme (project EP/S031170/1) and the University of Nottingham Propulsion Futures Beacon of Excellence for funding.

REFERENCES

(1) Gür, T. M. Review of Electrical Energy Storage Technologies, Materials and Systems: Challenges and Prospects for Large-Scale Grid Storage. *Energy Environ. Sci.* **2018**, *11* (10), 2696–2767. https://doi.org/10.1039/c8ee01419a.

(2) Trahey, L.; Brushett, F. R.; Balsara, N. P.; Ceder, G.; Cheng, L.; Chiang, Y. M.; Hahn, N. T.; Ingram, B. J.; Minteer, S. D.; Moore, J. S.; Mueller, K. T.; Nazar, L. F.; Persson, K. A.; Siegel, D. J.; Xu, K.; Zavadil, K. R.; Srinivasan, V.; Crabtree, G. W. Energy Storage Emerging: A Perspective from the Joint Center for Energy Storage Research. *Proc. Natl. Acad. Sci. U. S. A.* **2020**, *117* (23), 12550–12557. https://doi.org/10.1073/pnas.1821672117.

(3) Cameron, J. M.; Holc, C.; Kibler, A. J.; Peake, C. L.; Walsh, D. A.; Newton, G. N.; Johnson, L. R. Molecular Redox Species for Next-Generation Batteries. *Chem. Soc. Rev.* **2021**. *50*, 5863-5883. https://doi.org/10.1039/d0cs01507e.

(4) Rychcik, M.; Skyllas-Kazacos, M. Characteristics of a New All-Vanadium Redox Flow Battery. *J. Power Sources* **1988**, *22* (1), 59–67. https://doi.org/10.1016/0378-7753(88)80005-3.

(5) Dmello, R.; Milshtein, J. D.; Brushett, F. R.; Smith, K. C. Cost-Driven Materials Selection Criteria for Redox Flow Battery Electrolytes. *J. Power Sources* **2016**, *330*, 261–272. https://doi.org/10.1016/j.jpowsour.2016.08.129.

(6) *GRIDS: Grid-Scale Rampable Intermittent Dispatchable Storage*; United States Department of Energy, 2010. https://www.osti.gov/biblio/1046668.

(7) Lourenssen, K.; Williams, J.; Ahmadpour, F.; Clemmer, R.; Tasnim, S. Vanadium Redox Flow Batteries: A Comprehensive Review. *J. Energy Storage* **2019**, *25*, 100844. https://doi.org/10.1016/j.est.2019.100844.

(8) Hu, B.; DeBruler, C.; Rhodes, Z.; Liu, T. L. Long-Cycling Aqueous Organic Redox Flow Battery (AORFB) toward Sustainable and Safe Energy Storage. *J. Am. Chem. Soc.* **2017**, *139* (3), 1207–1214. https://doi.org/10.1021/jacs.6b10984.

(9) Hogue, R. W.; Toghill, K. E. Metal Coordination Complexes in Nonaqueous Redox Flow Batteries. *Curr. Opin. Electrochem.* **2019**, *18*, 37–45. https://doi.org/10.1016/j.coelec.2019.08.006.

(10) Ding, Y.; Zhang, C.; Zhang, L.; Zhou, Y.; Yu, G. Molecular Engineering of Organic Electroactive Materials for Redox Flow Batteries. *Chem. Soc. Rev.* **2018**, *47* (1), 69–103. https://doi.org/10.1039/c7cs00569e.

(11) Pratt, H. D.; Hudak, N. S.; Fang, X.; Anderson, T. M. A Polyoxometalate Flow Battery. *J. Power Sources* **2013**, *236*, 259–264. https://doi.org/10.1016/j.jpowsour.2013.02.056.

(12) Friedl, J.; Holland-Cunz, M. V; Cording, F.; Pfanschilling, F. L.; Wills, C.; McFarlane, W.; Schricker, B.; Fleck, R.; Wolfschmidt, H.; Stimming, U. Asymmetric Polyoxometalate Electrolytes for Advanced Redox Flow Batteries. *Energy Environ. Sci.* **2018**, *11* (10), 3010–3018. https://doi.org/10.1039/c8ee00422f.

(13) Chen, J. J.; Symes, M. D.; Cronin, L. Highly Reduced and Protonated Aqueous Solutions of $[P_2W_{18}O_{62}]^{6-}$ for on-Demand Hydrogen Generation and Energy Storage. *Nat. Chem.* **2018**, *10* (10), 1042–1047. https://doi.org/10.1038/s41557-018-0109-5.

(14) VanGelder, L. E.; Cook, T. R.; Matson, E. M. Progress in the Design of Polyoxovanadate-Alkoxides as Charge Carriers for Nonaqueous Redox Flow Batteries. *Comments Inorg. Chem.* **2019**, *39* (2), 51–89. https://doi.org/10.1080/02603594.2019.1587612.

(15) Friedl, J.; Pfanschilling, F. L.; Holland-Cunz, M. V.; Fleck, R.; Schricker, B.; Wolfschmidt, H.; Stimming, U. A Polyoxometalate Redox Flow Battery: Functionality and Upscale. *Clean Energy* **2019**, *3* (4), 278–287. https://doi.org/10.1093/ce/zkz019.

(16) Ejigu, A.; Greatorex-Davies, P. A.; Walsh, D. A. Room Temperature Ionic Liquid Electrolytes for Redox Flow Batteries. *Electrochem. Commun.* **2015**, *54*, 55–59. https://doi.org/10.1016/j.elecom.2015.01.016.

(17) Gong, K.; Fang, Q.; Gu, S.; Fong, S.; Li, Y.; Yan, Y. Nonaqueous Redox-Flow Batteries: Organic Solvents, Supporting Electrolytes, and Redox Pairs. *Energy Environ. Sci* **2015**, *8* (8), 3515–3530. https://doi.org/10.1039/c5ee02341f.

(18) Chen, J. J. J.; Barteau, M. A. Molybdenum Polyoxometalates as Active Species for Energy Storage in Non-Aqueous Media. *J. Energy Storage* **2017**, *13*, 255–261. https://doi.org/10.1016/j.est.2017.07.017.

(19) Cao, Y.; Chen, J. J. J.; Barteau, M. A. Systematic Approaches to Improving the Performance of Polyoxometalates in Non-Aqueous Redox Flow Batteries. *J. Energy Chem.* **2020**, *50*, 115–124. https://doi.org/10.1016/j.jechem.2020.03.009.

(20) Vangelder, L. E.; Kosswattaarachchi, A. M.; Forrestel, P. L.; Cook, T. R.; Matson, E. M. Polyoxovanadate-Alkoxide Clusters as Multi-Electron Charge Carriers for Symmetric Non-Aqueous Redox Flow Batteries. *Chem. Sci.* **2018**, *9* (6), 1692–1699. https://doi.org/10.1039/c7sc05295b.

(21) Vangelder, L. E.; Pratt, H. D.; Anderson, T. M.; Matson, E. M. Surface Functionalization of Polyoxovanadium Clusters: Generation of Highly Soluble Charge Carriers for Nonaqueous Energy Storage. *Chem. Commun.* **2019**, *55* (81), 12247–12250. https://doi.org/10.1039/c9cc05380h.

(22) VanGelder, L. E.; Petel, B. E.; Nachtigall, O.; Martinez, G.; Brennessel, W. W.; Matson, E. M. Organic Functionalization of Polyoxovanadate–Alkoxide Clusters: Improving the Solubility of Multimetallic Charge Carriers for Nonaqueous

Redox Flow Batteries. *ChemSusChem* **2018**, *11* (23), 4139–4149. https://doi.org/10.1002/cssc.201802029.

(23) VanGelder, L. E.; Pratt, H. D.; Anderson, T. M.; Matson, E. M. Surface Functionalization of Polyoxovanadium Clusters: Generation of Highly Soluble Charge Carriers for Nonaqueous Energy Storage. *Chem. Commun.* **2019**, *55* (81), 12247–12250. https://doi.org/10.1039/c9cc05380h.

(24) Kibler, A. J.; Newton, G. N. Tuning the Electronic Structure of Organic–Inorganic Hybrid Polyoxometalates: The Crucial Role of the Covalent Linkage. *Polyhedron* **2018**, *154*, 1–20. https://doi.org/10.1016/j.poly.2018.06.027.

(25) Song, Y. F.; Tsunashima, R. Recent Advances on Polyoxometalate-Based Molecular and Composite Materials. *Chem. Soc. Rev.* **2012**, *41* (22), 7384–7402. https://doi.org/10.1039/c2cs35143a.

(26) Wales, D. J.; Cao, Q.; Kastner, K.; Karjalainen, E.; Newton, G. N.; Sans, V. 3D-Printable Photochromic Molecular Materials for Reversible Information Storage. *Adv. Mater.* **2018**, *30* (26), 1800159. https://doi.org/10.1002/adma.201800159.

(27) Hampson, E.; Cameron, J. M.; Amin, S.; Kyo, J.; Watts, J. A.; Oshio, H.; Newton, G. N. Asymmetric Hybrid Polyoxometalates: A Platform for Multifunctional Redox-Active Nanomaterials. *Angew. Chem. Int. Ed.* **2019**, *58* (50), 18281–18285. https://doi.org/10.1002/anie.201912046.

(28) Hampson, E.; Cameron, J. M.; Watts, J. A.; Newton, G. N. Transition Metal Decorated Soft Nanomaterials through Modular Self-Assembly of an Asymmetric Hybrid Polyoxometalate. *Chem. Commun.* **2020**, *56* (59), 8237–8240. https://doi.org/10.1039/d0cc03554h.

(29) Amin, S.; Cameron, J. M.; Watts, J. A.; Walsh, D. A.; Sans, V.; Newton, G. N. Effects of Chain Length on the Size, Stability, and Electronic Structure of Redox-Active Organic-Inorganic Hybrid Polyoxometalate Micelles. *Mol. Syst. Des. Eng.* **2019**, *4* (5), 995–999. https://doi.org/10.1039/c9me00060g.

(30) Kibler, A. J.; Martín, C.; Cameron, J. M.; Rogalska, A.; Dupont, J.; Walsh, D. A.; Newton, G. N. Physical and Electrochemical Modulation of Polyoxometalate Ionic Liquids via Organic Functionalization. *Eur. J. Inorg. Chem.* **2019**, *3–4*, 456–460. https://doi.org/10.1002/ejic.201800578.

(31) Piot, M.; Abécassis, B.; Brouri, D.; Troufflard, C.; Proust, A.; Izzet, G. Control of the Hierarchical Self-Assembly of Polyoxometalate-Based Metallomacrocycles by Redox Trigger and Solvent Composition. *Proc. Natl. Acad. Sci. U. S. A.* **2018**, *115* (36), 8895–8900. https://doi.org/10.1073/pnas.1808445115.

(32) Boujtita, M.; Boixel, J.; Blart, E.; Mayer, C. R.; Odobel, F. Redox Properties of Hybrid Dawson Type Polyoxometalates Disubstituted with Organo-Silyl or Organo-Phosphoryl Moieties. *Polyhedron* **2008**, *27* (2), 688–692. https://doi.org/10.1016/j.poly.2007.10.022.

(33) Compton, R.; Banks, C. *Understanding Voltammetry*, 3rd ed.; World Scietific Publishing Europe Ltd.: New Jersey, 2018.

(34) Sum, E.; Skyllas-Kazacos, M. A Study of the V(II)/V(III) Redox Couple for Redox Flow Cell Applications. *J. Power Sources* **1985**, *15* (2–3), 179–190. https://doi.org/10.1016/0378-7753(85)80071-9.

(35) Liu, Q.; Sleightholme, A. E. S.; Shinkle, A. A.; Li, Y.; Thompson, L. T. Non-Aqueous Vanadium Acetylacetonate Electrolyte for Redox Flow Batteries. *Electrochem. Commun.* **2009**, *11* (12), 2312–2315. https://doi.org/10.1016/j.elecom.2009.10.006.

(36) Nicholson, R. S. Theory and Application of Cyclic Voltammetry for Measurement of Electrode Reaction Kinetics. *Anal. Chem.* **1965**, *37* (11), 1351–1355. https://doi.org/10.1021/ac60230a016.

(37) Goulet, M.-A.; Aziz, M. J. Flow Battery Molecular Reactant Stability Determined by Symmetric Cell Cycling Methods. *J. Electrochem. Soc.* **2018**, *165* (7), A1466–A1477. https://doi.org/10.1149/2.0891807jes.

(38) Armstrong, C. G.; Hogue, R. W.; Toghill, K. E. Characterisation of the Ferrocene/Ferrocenium Ion Redox Couple as a Model Chemistry for Non-Aqueous Redox Flow Battery Research. *J. Electroanal. Chem.* **2020**, *872*, 114241. https://doi.org/10.1016/j.jelechem.2020.114241.

(39) Friedl, J.; Holland-Cunz, M. V.; Cording, F.; Pfanschilling, F. L.; Wills, C.; McFarlane, W.; Schricker, B.; Fleck, R.; Wolfschmidt, H.; Stimming, U. Asymmetric Polyoxometalate Electrolytes for Advanced Redox Flow Batteries. *Energy Environ. Sci.* **2018**, *11* (10), 3010–3018. https://doi.org/10.1039/c8ee00422f.

(40) Varga, G. M.; Papaconstantinou, E.; Pope, M. T. Heteropoly Blues. IV. Spectroscopic and Magnetic Properties of Some Reduced Polytungstates1. *Inorg. Chem.* **1970**, *9* (3), 662–667. https://doi.org/10.1021/ic50085a045.

For Table of Contents only.